

Nontrivial scaling in supply limited Aeolian sand transport

Sandesh Kamath^{1,1,1}, Yaping Shao^{2,2,2}, and Eric Ribeiro Parteli^{3,3,3}

¹Institute of Geophysics and Meteorology, University of Cologne

²University of Cologne

³University of Duisburg-Essen

November 30, 2022

Abstract

Previous studies of wind-blown sand have considered either fully erodible or non-erodible soils, but the transport over sparsely sand-covered soils is still poorly understood. The quantitative modeling of this transport is important for the parametrization of Aeolian processes under low sand availability. Here we show, by means of particle-based numerical simulations, that the Aeolian sand transport rate Q scales with the wind shear velocity u^* as $Q = a \cdot [1 + b \cdot (u^*/u^*_{*t} - 1)] \cdot (d/g) \cdot \rho_f \cdot (u^{*2} - u^{*t2})$, where u^*_{*t} is the minimal threshold u^* for sustained transport, d is particle size, g is gravity and ρ_f is air density, while u^*_{*t} and the empirical parameters a and b depend on the sand cover thickness. Our model explains the transition from the quadratic to cubic scaling of Q with u^* as soil conditions change from fully erodible to rigid and provides constraints for modeling Aeolian transport under low sand availability.

Scaling laws in Aeolian sand transport under low sand availability

Sandesh Kamath^{1,2}, Yaping Shao¹, Eric J. R. Parteli²

¹Institute of Geophysics and Meteorology, University of Cologne, Germany

²Faculty of Physics, University of Duisburg-Essen, Germany

Key Points:

- We introduce a particle-based model in investigating Aeolian (wind-blown) sand transport when the sand cover on the soil is sparse
- The scaling of the Aeolian transport rate with the wind shear velocity has a dependency on the sand cover thickness
- There is an anomaly in the functional dependence of the transport rate on the sand cover thickness, depending on the rigid ground roughness

Corresponding author: Sandesh Kamath, skamath@uni-koeln.de

Abstract

Previous studies of wind-blown sand have considered either fully erodible or non-erodible soils, but the transport over sparsely sand-covered soils is still poorly understood. The quantitative modeling of this transport is important for parameterizing Aeolian processes under low sand availability. Here we show, by means of numerical simulations, that the sand transport rate Q scales with the wind shear velocity u_* as $Q = a \cdot [1 + b \cdot (u_*/u_{*t} - 1)] \cdot \sqrt{d/g} \cdot \rho_f \cdot (u_*^2 - u_{*t}^2)$, where u_{*t} is the minimal threshold u_* for sustained transport, d is particle size, g is gravity and ρ_f is air density, while u_{*t} and the empirical parameters a and b depend on the sand cover thickness. Our model explains the transition from the quadratic to cubic scaling of Q with u_* as soil conditions change from fully erodible to rigid and provides constraints for modeling Aeolian transport under low sand availability.

Plain Language Summary

The transport of sand by wind shapes the Earth's surface and constitutes one major factor for the emission of dust aerosols. The accurate modeling of wind-blown sand transport is thus important to achieve reliable climate simulations and to make predictions about the propagation of desertification. Previous models of wind-blown sand were designed to compute sand transport rates over a thick sand layer, such as the surface of large, active sand dunes. However, natural soils encompass a broad range of low sand availability conditions, such as crusted or bare soils. It has been a long-standing open question how wind-blown sand transport rates respond to wind velocity when the bare ground is covered by a thin layer of sand. Here we calculate the trajectories of wind-blown sand grains and find that sand transport rates increase faster with wind speed under low sand availability conditions than over sand dunes. The reason for this behavior is elucidated in our simulations: The hopping sand grains fly higher the less sand is covering the hard surface. We obtain mathematical expressions for the sand transport rates as a function of the thickness of sand covering the bare soil, which will be important to improve climate models.

1 Introduction

Aeolian (wind-blown) sand transport produces ripples and dunes and plays a vital role in shaping the Earth's surface. This transport occurs mainly through sand grains hopping along the surface (saltation), thereby transferring to the ground momentum that may set new particles into hopping, rolling or sliding motion (Bagnold, 1941; Shao, 2008; Kok et al., 2012). Furthermore, the particle splash generated by saltating grains provides one main mechanism of dust aerosol emission (Gillette, 1981; Shao et al., 1993), which has major feedbacks with the biosphere, the hydrological cycle and various other components of the Earth system (Mahowald et al., 2014; Schepanski, 2018). The accurate modeling of wind-blown sand is, thus, important for the development of reliable geomorphodynamic, climate and Earth system models (Shao, 2008).

Indeed, previous models of Aeolian transport focused mainly on the transport over either fully erodible beds, such as migrating dunes and ripples (Anderson & Haff, 1988; Shao & Li, 1999; Sauermann et al., 2001; Almeida et al., 2008; Kok & Renno, 2009; Lämmel et al., 2012; Pähtz et al., 2014; Comola et al., 2019), or rigid, fully non-erodible beds, such as consolidated dunes and bare soils (Ho et al., 2011). These studies have shown that wind-blown transport rates follow either a quadratic or a cubic scaling with the wind shear velocity u_* — which is proportional to the mean flow velocity gradient in turbulent boundary layer flow — depending upon the bed being fully erodible or fully non-erodible, respectively (Creyssels et al., 2009; Ho et al., 2011). Moreover, a quartic scaling of the sand flux with u_* , characterizing a collisional or intense transport regime where the saltation layer is connected to the granular bed through an intermediate granular layer of intense mid-air collisions, has been reported for fully erodible bed conditions when u_* exceeds about $4u_{*t}$,

62 where u_{*t} stands for the minimal threshold for sustained transport (Pächtz & Durán, 2020;
 63 Ralaiarisoa et al., 2020). However, natural Aeolian systems encompass a broad range of soil
 64 types characterized by low sand availability on the ground, including bare and crusted soils
 65 sparsely covered with mobile sediments (Shao, 2008; Amir et al., 2014). The characteristics
 66 of Aeolian transport over such types of soil, i.e., when the thickness of the mobile sand layer
 67 on the rigid ground is comparable to a few grain diameters, are poorly understood.

68 The quantitative understanding of these characteristics is important for various fields, in
 69 particular to improving wind-blown sand and dust schemes in climate models. Once in the
 70 atmospheric circulation, dust substantially affects the planet’s climate and biosphere, at-
 71 mospheric geochemistry, the hydrological cycle, and various other components of the Earth
 72 system, yet estimates of vertical dust flux and atmospheric dust budget are counted amongst
 73 the largest uncertainty sources in climate simulations (Shao, 2008; Kok et al., 2012; Ma-
 74 howald et al., 2014; Schepanski, 2018). Since dust is rarely entrained directly by wind but is,
 75 instead, emitted mainly by the impacts of wind-blown sand grains onto the ground (Shao et
 76 al., 1993), an accurate model for the Aeolian sand transport rates over various types of soil,
 77 from fully erodible to fully non-erodible, is required. However, it is difficult to derive such a
 78 model from analytical computations alone, given the broad range of natural soil erodibility
 79 conditions associated with sparsely covered bare, gravel and crusted soils (Shao, 2008; Amir
 80 et al., 2014; Macpherson et al., 2008; Wang et al., 2011).

81 Therefore, here we perform the direct computation of grain trajectories during Aeolian sand
 82 transport by means of particle-based simulations, or Discrete-Element-Method (DEM). This
 83 type of simulation has been applied previously to investigate Aeolian transport over fully
 84 erodible beds (Carneiro et al., 2011; Durán et al., 2012; Comola et al., 2019), thereby
 85 introducing a helpful means to elucidate processes that are difficult to assess in wind tunnel
 86 or field experiments, such as the mechanisms of sediment transport very close to the bed.
 87 Indeed, using DEM simulations, it is possible to resolve these mechanisms, as well as their
 88 impact on the resulting sand flux, without any need for assumptions about the splash
 89 process, the rebound dynamics or the modification of the wind profile in the transport
 90 layer – which are rather directly computed. As we discuss in the subsequent sections, our
 91 DEM simulations show that the scaling of the sand flux with u_* displays considerable and
 92 yet unreported dependence on the availability of sand on the ground — characterized here
 93 through the thickness of the mobile sediment layer covering the non-erodible surface.

94 **2 Numerical experiments**

95 The Discrete-Element-Method consists of solving Newton’s equations of motion for all par-
 96 ticles in the system under consideration of the main forces acting on them (Cundall &
 97 Strack, 1979). In contrast to other types of numerical models of soil erosion (Anderson
 98 & Haff, 1988; Almeida et al., 2008; Kok & Renno, 2009), DEM models of Aeolian trans-
 99 port do not rely, thus, on a splash function to represent the ejection of particles from the
 100 soil owing to grain-bed collisions. Rather, the lift-off velocities of the rebound and ejected
 101 particles are obtained by directly solving their equations of motion under consideration of
 102 particle-particle interactions (Lämmel et al., 2017; Yin et al., 2021).

103 We start our simulations by pouring sand-sized spherical particles of diameter d uniformly
 104 distributed in the range $160 \leq d/\mu\text{m} \leq 240$ onto a flat horizontal rigid bed at the bottom of
 105 the simulation domain — which has dimensions $(L_x \times L_y \times L_z)/d_m = (200 \times 8 \times 1000)$, with
 106 $d_m = 200 \mu\text{m}$ denoting the mean grain size (Fig. 1). In doing so, we generate a thin bed of
 107 N_p randomly poured particles on the ground, where the bed thickness δ_0 is determined by
 108 N_p . For instance, $N_p = 30,000$ for $\delta_0 \approx 15 d_m$.

109 Furthermore, we adopt periodic boundary conditions in the along-wind (x) and cross-wind
 110 (y) directions and impose a reflective horizontal wall at the top of the simulation domain,
 111 to avoid that particles escape through crossing the upper boundary at $z = L_z$. However,

112 we find that removing this reflective wall would allow only few particles for escaping, thus
 113 leading to a negligible change in the results of our simulations.

114 Once the particles come to rest and the bed has been formed, a few particles are injected
 115 into the simulation domain to impact on the ground, thus producing a splash and ejecting
 116 grains into air. The Aeolian drag force on the particles is computed with the expression,

$$117 \quad \mathbf{F}_i^d = -\frac{\pi d_i^2}{8} \rho_f C_i^d v_i^r \mathbf{v}_i^r, \quad (1)$$

118 where $\rho_f = 1.225 \text{ kg/m}^3$ is the air density and $\mathbf{v}_i^r = \mathbf{v}_i - \mathbf{u}(z_i)$ is the difference between
 119 the velocity \mathbf{v}_i of particle i and the wind velocity $\mathbf{u}(z_i)$ at the height z_i of the particle's
 120 center of mass. Furthermore, $v_i^r = |\mathbf{v}_i^r|$, while the drag coefficient C_i^d is computed through
 121 (Cheng, 1997) $C_i^d = \left[(32/\text{Re}_i)^{2/3} + 1 \right]^{3/2}$, where the Reynolds number $\text{Re}_i = \rho_f v_i^r d_i / \mu$,
 122 with $\mu = 1.8702 \times 10^{-5} \text{ kg m}^{-1} \text{ s}^{-1}$ denoting the dynamic viscosity of the air.

123 The wind velocity profile is constant along x and y throughout the simulations, while
 124 the initial vertical profile of the horizontal (downstream) wind velocity, $u_x(z)$, reads,

$$125 \quad u_x(z) = \frac{u_*}{\kappa} \ln \frac{z - h_0 + z_0}{z_0} \quad (2)$$

126 where u_* is the wind shear velocity, $\kappa = 0.4$ the von Kármán constant, $z_0 \approx d_m/30$ is
 127 the roughness of the quiescent bed, and h_0 is the bed height, which is set as the uppermost
 128 height within the granular surface where the particles move with velocity smaller than $0.1 u_*$
 129 (Carneiro et al., 2011). However, the acceleration of the particles owing to the action of
 130 the drag force extracts momentum from the air (Owen, 1964; Anderson & Haff, 1988),
 131 thus leading to a modification of the wind velocity profile. The modified velocity profile is
 132 obtained by numerical integration of (Carneiro et al., 2011)

$$133 \quad \frac{\partial u_x}{\partial z} = \frac{u_{\tau,x}(z)}{\kappa z}; \quad u_{\tau,x}(z) = u_* \left[1 - \frac{\tau_p(z)}{\rho_f u_*^2} \right]^{1/2}, \quad (3)$$

134 where $\tau_p(z)$ is the grain-borne shear stress and is given by

$$135 \quad \tau_p(z) \approx \sum_{j:Z_j>z} \frac{\mathcal{F}_x^d(Z_j)}{A}, \quad (4)$$

136 with $\mathcal{F}_x^d(Z_j)$ denoting the horizontal component of the total drag force on the particles with
 137 center of mass at Z_j , while $A = L_x \cdot L_y$ (Carneiro et al., 2011).

138 Furthermore, in order to obtain a rough rigid bed underneath the mobile sand cover, we
 139 deposit the mobile particles on top of a sheet of “frozen” immobile particles as displayed in
 140 Fig. 1 (see Suppl. Mat. for the set of DEM particle-particle contact force equations, including
 141 the presence of the frozen particles). In doing so, the rigid bed provides a model for a fully
 142 consolidated dune surface or bare granular surface, where the constituent immobile particles
 143 have the same diameter as the mobile grain size.

144 3 Results and discussion

145 Once transport begins, some of the grains composing the initial bed layer are entrained
 146 into flow, so that the bed layer thickness — which has initial value δ_0 at time $t = 0$ —
 147 decreases over time until transport eventually achieves steady state. At steady state, the
 148 bed layer thickness amounts to $\delta_s/d_m = (\delta_0/d_m - C_b u_* / \sqrt{g d_m}) \cdot \Theta(\delta_0/d_m - C_b u_* / \sqrt{g d_m})$,
 149 where $C_b \approx 0.02$ is an empirical parameter and $\Theta(x)$ denotes the Heaviside function, i.e.,
 150 $\Theta(x) = 1$ if $x \geq 0$ and $\Theta(x) = 0$ if $x < 0$ (see Fig. S3). Therefore, the term $C_b u_* / (\sqrt{g d_m})$

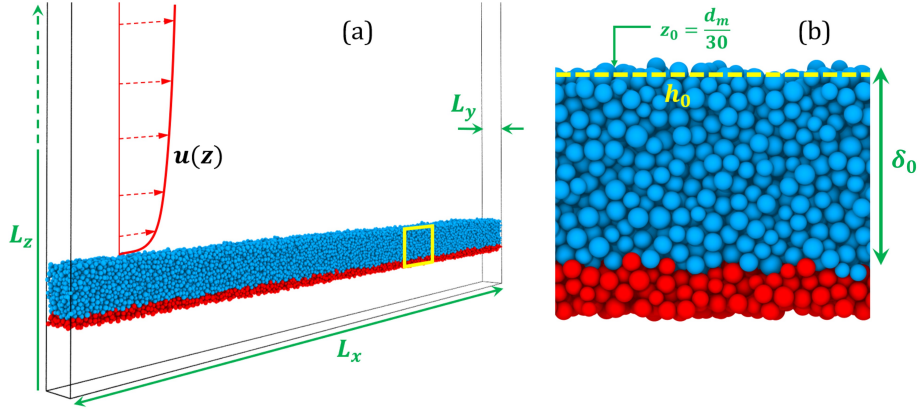


Figure 1: (a) Snapshot of the numerical experiment at $t = 0$, indicating the dimensions of the simulation domain and the undisturbed wind profile. (b) Side-view of an excerpt of the sediment bed, displaying a layer of mobile particles (blue) of thickness δ_0 on top of the immobile particles constituting the rough ground.

151 ($\lesssim 0.5$ for all scenarios) denotes the thickness of the total eroded layer, relative to the
 152 particle size, from the beginning of transport until steady state.

153 We note that periodic boundary conditions are applied in our simulations (see Section 2),
 154 so that the number of particles in the system is constant over time (Carneiro et al., 2011;
 155 Durán et al., 2012; Pätz & Durán, 2020). Indeed, the domain of our simulations may be
 156 interpreted as a small stretch of soil over which the sediment flux is in the steady state. Due
 157 to fluctuations associated with the transport dynamics, the difference between the particle
 158 mass outflux from and influx into this soil stretch varies over time, but on average, the total
 159 number of particles within the associated volume is constant over time.

160 We begin our discussion by considering an initial bed thickness $\delta_0 = 15 d_m$, for which we
 161 observe steady-state transport conditions ($\delta_s \approx 14.8 d_m$) consistent with the fully erodible
 162 bed scenario reported in previous studies. Specifically, our simulations reproduce quanti-
 163 tatively the height-integrated, non-suspended mass flux of transported particles, Q , as a
 164 function of u_* over fully erodible beds, and the observation that, for moderate wind condi-
 165 tions ($u_*/u_{*t} \lesssim 4$), Q is approximately proportional to $\tau - \tau_t$, with $\tau = \rho_f u_*^2$ denoting the
 166 mean shear stress of the turbulent wind flow over the surface, and $\tau_t = \rho_f u_{*t}^2$ corresponding
 167 to the minimal threshold τ for transport (Fig. 2). Furthermore, our numerical predictions
 168 match the experimental observations of the nearly exponential decay of the vertical particle
 169 concentration with the height above the ground and the value of $u_{*t} \approx 0.165$ m/s predicted
 170 for the mean particle size in our simulations (see Suppl. Mat., Fig. S1).

171 However, as we decrease the initial bed layer thickness δ_0 substantially, we observe a change
 172 in the scaling of the steady-state sediment flux with u_* . More precisely, our simulation
 173 results follow, approximately, the model,

$$Q = \left\{ a \cdot \left[1 + b \cdot \left(\frac{u_*}{u_{*t}} - 1 \right) \right] \right\} \cdot \sqrt{\frac{d}{g}} \cdot [\tau - \tau_t], \quad (5)$$

$$u_{*t} = u_{*t,\infty} \cdot \{ 1 - C_t \cdot \exp[-c_t \cdot \delta_s/d_m] \} \quad (6)$$

$$a = a_\infty \cdot \{ 1 - C_a \cdot \exp[-c_a \cdot \delta_s/d_m] \} \quad (7)$$

$$b = b_\infty \cdot \exp[-c_b \sqrt{\delta_s/d_m}] \quad (8)$$

174 where $u_{*t,\infty} \approx 0.165$ m/s, $a_\infty \approx 22.15$ and $b_\infty \approx 5.28$ denote the values of u_{*t} and the empir-
 175 ical constants a and b , respectively, associated with fully erodible bed scenario ($\delta_s/d_m \rightarrow \infty$),
 176 while the best fits to the simulation data in the range $\delta_s/d_m \leq 10$ yield $C_t \approx 0.14$, $c_t \approx 0.83$,
 177 $C_a \approx 0.47$, $c_a \approx 0.76$ and $c_b \approx 2.61$ (Fig. 2).

178 Wind tunnel experiments (Ho et al., 2011) revealed a cubic scaling of Q with u_* on fully
 179 rigid beds. Here, we find that sediment transport rates over a soil that is not fully rigid but
 180 contains, instead, a thin layer of mobile sediment, further depends on this layer's thickness
 181 according to Eqs. (5)-(8). Specifically, the coefficient b in Eq. (8) controls the transition
 182 from the cubic to the quadratic scaling of Q with u_* in Eq. (5) as bed conditions change
 183 from fully rigid ($\delta_s = 0$) to fully erodible ($\delta_s \gg d$). Moreover, while the coefficient a provides
 184 an attenuating factor for Q near the rigid bed scenario, a decrease in bed thickness reduces
 185 the minimal threshold shear velocity, u_{*t} , as we elucidate next.

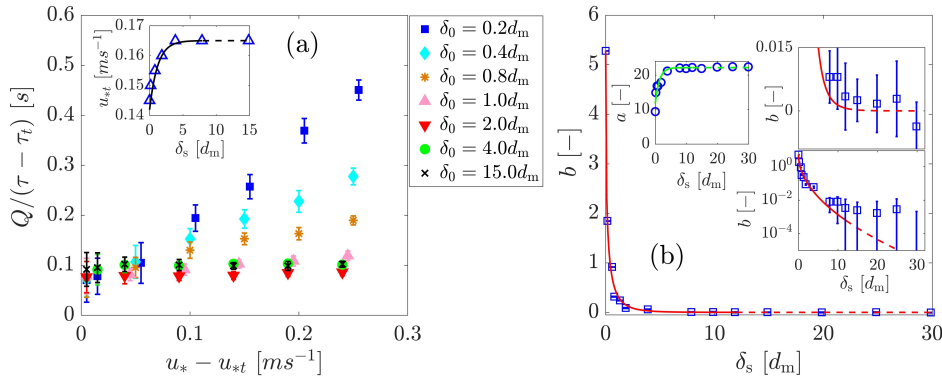


Figure 2: (a) Sand flux Q rescaled with the excess shear stress, $\tau - \tau_t$, plotted as a function of $(u_* - u_{*t})$ for different values of the initial bed thickness, δ_0 ; inset: the minimal threshold shear velocity for sustained transport, u_{*t} as a function of the steady-state bed thickness, δ_s . (b) Circles and squares denote the parameters a and b in Eq. (5), respectively, as obtained from the best fit to the data in (a). The continuous lines in (a) and (b) denote the best fits using Eqs. (6)-(8) in the range $\delta_s/d_m \leq 10$ (the continuation of these fits toward larger δ_s/d_m or fully erodible bed scenario is indicated by the dashed line as a guide to the eye). Error bars denote the standard deviation from averaging over 5 s within the steady state.

186 To shed light on the microscopic origin of Eq. (5), we note that momentum conservation
 187 yields $Q = [\ell_{\text{hop}}/(u_{0\downarrow} - u_{0\uparrow})] \cdot [\tau - \tau_t]$ (Bagnold, 1941; Sørensen, 2004; Ho et al., 2011),
 188 where ℓ_{hop} denotes the mean hop length of the saltating particles, while $u_{0\downarrow}$ and $u_{0\uparrow}$ are
 189 their mean horizontal impact and lift-off velocities, respectively. Furthermore, ℓ_{hop} and
 190 $u_{0\downarrow} - u_{0\uparrow}$ (computed as explained in Section 4 of the Suppl. Mat.) are related to the mean
 191 horizontal grain velocity $u_0 = (u_{0\downarrow} + u_{0\uparrow})/2$ (or slip velocity) through the approximate
 192 scaling expressions $\ell_{\text{hop}} \propto u_0^2/g$ and $u_{0\downarrow} - u_{0\uparrow} \propto u_0$ (Ho et al., 2011), which leads to
 193 $Q \approx C_u \cdot (u_0/g) \cdot [\tau - \tau_t]$, where C_u is an empirical parameter.

194 An increase in u_* over a fully erodible bed leads to an enhancement of the particle concentra-
 195 tion in the transport layer without significantly affecting u_0 , so that Q scales quadratically
 196 with u_* in the fully erodible bed regime (Ho et al., 2011). By contrast, the transport layer
 197 over the hard surface is, for a given saltation flux, much thicker than over an erodible bed
 198 because of the non-saturated feedback which keeps a larger wind velocity in the saltation
 199 layer (Ho et al., 2011). The weak coupling between the particles and the wind in the trans-
 200 port layer over a fully non-erodible surface results in a linear scaling of u_0 with u_* , thus
 201 yielding a cubic scaling of Q with u_* in the fully rigid bed regime (Ho et al., 2011).

202 Here we find that, in the presence of a thin layer of mobile sand on the hard ground, the
 203 scaling of u_0 with u_* further depends on δ_s (Fig. 3c). We find that

$$204 \quad C_u \cdot \frac{u_0}{g} \approx a \cdot \left[1 + b \cdot \left(\frac{u_*}{u_{*t}} - 1 \right) \right] \sqrt{\frac{d}{g}} \quad (9)$$

205 with $C_u \approx 1.68$, where the RHS of Eq. (9) is the multiplicative factor of $[\tau - \tau_t]$ in Eq. (5),
 206 i.e., including the values of u_{*t} , a and b estimated from Fig. 2. Therefore, Eq. (9) elucidates
 207 the microscopic origin of Eq. (5). Since all scenarios (δ_0 , u_*) considered here are associated
 208 with saturated transport conditions in the steady state (see Suppl. Mat., Fig. S3), i.e., since
 209 the total mass of particles in the transport layer under given $u_* - u_{*t}$ is the same for all
 210 values of δ_0 considered, the effect of sand availability on the scaling of $Q(u_*)$ is attributed
 211 entirely to the dependence of u_0 on this availability, encoded in the parameters on the
 212 RHS of Eq. (9). Our simulations further show that, as sand availability decreases and the
 213 transport layer expands, transport can be sustained at increasingly lower u_* (Fig. 2a and
 214 Eq. (6)). This finding is further consistent with the wind-tunnel observation that u_{*t} over
 215 fully rigid beds is lower than over fully erodible beds (Ho et al., 2011).

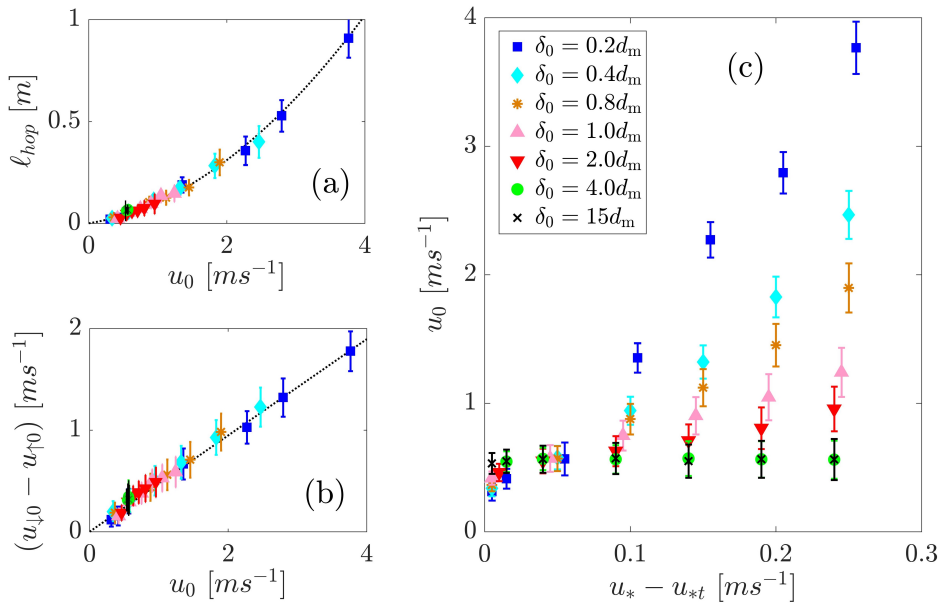


Figure 3: (a) Mean hop length, ℓ_{hop} , and (b) difference between the mean grain horizontal velocities at impact and lift-off, $u_{0\downarrow} - u_{0\uparrow}$, as a function of the slip velocity u_0 . The dashed lines in (a) and (b) denote $\ell_{\text{hop}} \approx 0.065u_0^2$ and $u_{0\downarrow} - u_{0\uparrow} \approx 0.43u_0$, respectively, obtained from the best fits to the simulation data. In (c), the slip velocity is shown as a function of $u_* - u_{*t}$ for different values of δ_0 . The legend in (c) applies as well to both (a) and (b).

216 To the best of our knowledge, our study is the first one to estimate sediment transport rates
 217 from direct numerical simulations of particle trajectories under intermediate soil erodibility
 218 conditions between fully erodible and fully non-erodible. We find that our results remain
 219 approximately valid when the rigid bed underneath the mobile sediment layer is a smooth
 220 flat surface. However, the immobile roughness elements on the hard ground have a crucial
 221 effect on the value of the Aeolian sand flux.

222 In the regime where saltating particles collide onto a sand bed of thickness $\lesssim 2d_m$, and
 223 in the presence of roughness elements on the hard ground underneath, sand particles are

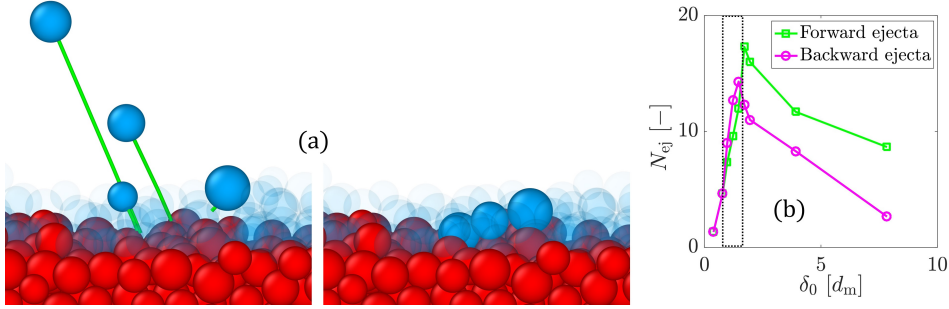


Figure 4: By means of granular splash numerical experiments with impact angles and velocities characteristic of wind-blown sand transport (a), we find that most ejected grains have negative horizontal lift-off velocity, when the value of the bed layer thickness is $\lesssim 2 d_m$, and positive otherwise (b). The snapshots correspond to a simulation using a bed layer thickness $\approx 2 d_m$. Most of the mobile (blue) particles lying on the rigid grains (red) have been rendered transparent for better visualization of the splashed particles.

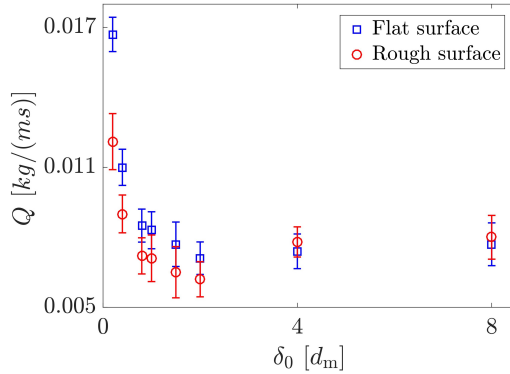


Figure 5: Sand flux Q as a function of δ_0 , obtained with $u_* = 0.30$ m/s. We considered the non-erodible surface consisting of a smooth flat ground (blue) and immobile particles (red).

224 ejected through splash events mainly *backwards*, i.e., the majority of ejecta displays nega-
 225 tive horizontal lift-off velocity component. This result can be understood by noting that,
 226 as downwind hopping grains impact obliquely upon the thin sand layer covering the rough
 227 ground, they mobilize soil grains forward, which, however, collide with the roughness el-
 228 ements located in their front. Upon such collisions, the trajectories of the bed particles
 229 mobilized by grain-bed impacts are reflected backwards, as elucidated through our granular
 230 splash experiments (Fig. 4, where N_{ej} is the number of ejected grains per impact).

231 These dynamics, which act by attenuating Q upon exposure of the bed roughness elements,
 232 are encoded in the coefficient a in Eq. (5), and constitute behavior opposite to the effect of
 233 the bed thickness on b and u_{*t} , which contribute to enhancing Q (see Eqs. (5)-(8)). These
 234 competing effects lead to an anomaly in the dependence of Q on the bed thickness, with the
 235 emergence of a minimum around $\delta_0 \approx 2 d_m$ (or $\delta_s \approx 1.8 d_m$). This anomaly is not observed
 236 when the ground is a smooth flat surface (Fig. 5). The bed thickness associated with the
 237 minimum Q is independent of u_* , thus indicating that the anomaly reported here is purely
 238 a signature of the bed roughness and is not affected by the flow properties.

239 We note that, notwithstanding the strong decrease of N_{ej} with the bed thickness in the
 240 regime $\delta_0/d_m \gtrsim 2$ (Fig. 4b), the steady-state sand flux Q in this regime is only weakly

241 affected by the amount of mobile grains on the ground (Fig. 2a). Therefore, our simulation
242 results are providing evidence in support of the hypothesis that the magnitude of Q is
243 controlled by the rebound dynamics of sand grains during transport — as assumed, for
244 instance, in a recent purely rebound-based model (Pächtz et al., 2021) — rather than by the
245 splash process. Our results further help to elucidate the observation that cohesion, which
246 affects mainly the splash process by enhancing particle-particle attractive interaction forces
247 within the bed, has little impact on Q and the threshold for Aeolian transport cessation, as
248 these are mainly controlled by rebound dynamics (Comola et al., 2019).

249 Our model reproduces the scaling laws of Q with u_* observed experimentally over fully
250 erodible and rigid beds (Figs. 2 and S1). However, various ingredients that are essential to
251 improve the quantitative assessment of Aeolian sand flux, such as complex particle geometric
252 shapes and aerodynamic entrainment (Li et al., 2020), should be incorporated in future
253 work. Furthermore, we have employed sand-sized non-erodible roughness elements, but
254 natural soils encompass much broader particle size distributions, including gravels, pebbles
255 and rocks. From our results, we expect that such coarser non-erodible elements have even
256 larger impact on the sand flux scaling. Our model is paving the way toward a quantitative
257 representation of sand availability conditions in larger scale models, such as regional Earth
258 system simulations, by explicitly incorporating the information of local steady-state bed
259 thickness in the parameterization of Aeolian sand transport rates.

260 Previous work developed continuum models for Aeolian flux that explicitly account for sand
261 supply and spatio-temporal variations in bed surface properties, including moisture, shells,
262 non-erodible elements and vegetation (De Vries et al., 2014; Hoonhout & Vries, 2016). Fur-
263 thermore, the particle-based simulations adopted in the present work provide a means to
264 improve our understanding of the (microscopic) particle-scale mechanisms controlling the re-
265 sponse of Aeolian transport processes to different types of soil and particle-bed interactions.
266 Future research combining insights from both types of model could thus help to achieve
267 improved numerical simulations of Aeolian soil morphodynamic processes at different scales
268 (Werner, 1995; Kroy et al., 2002; Durán et al., 2010), by incorporating the effect of sediment
269 availability on sediment flux and erosion/deposition rates.

270 4 Conclusions

271 In conclusion, we have presented the first numerical model for wind-blown sand flux under
272 low sand availability, by characterizing this flux as a function of the thickness of the mobile
273 sediment layer available for transport on the ground. Specifically, we showed that the
274 Aeolian sand flux scales with the excess shear stress multiplied by a coefficient that decreases
275 with the mobile layer thickness covering the non-erodible ground, thereby yielding a model
276 for Aeolian transport rates under intermediate bed erodibility conditions between the fully
277 erodible and fully non-erodible scenarios. Our model elucidates how the scaling of the
278 Aeolian sand flux Q with the wind shear velocity u_* changes from quadratic to cubic as bed
279 conditions change from fully erodible to fully non-erodible, respectively (Ho et al., 2011).

280 We also found that the roughness elements on the rigid bed affect the sediment flux upon
281 rigid bed exposure, by causing an anomaly in the behavior of Q with the bed layer thickness,
282 with the occurrence of a minimum which is independent on the flow conditions. These
283 findings will have an implication for the representation of non-erodible elements associated
284 with different types of soil in future experimental and theoretical studies.

285 5 Open Research

286 All data included in this work are generated from our numerical model and is available online
287 (<https://doi.org/10.6084/m9.figshare.19469501>). The data for validation with experiments
288 is available from (Creysseles et al., 2009).

289 **Acknowledgments**

290 We thank the German Research Foundation (DFG) for funding through the Heisenberg
 291 Programme and the grant - 348617785. We also thank Sierd de Vries and an anonymous
 292 reviewer for comments and suggestions that contributed much to improving this manuscript.

293 **References**

- 294 Almeida, M. P., Parteli, E. J. R., Andrade, J. S., & Herrmann, H. J. (2008). Giant saltation
 295 on mars. *Proceedings of the National Academy of Sciences*, *105*(17), 6222–6226. doi:
 296 <https://doi.org/10.1073/pnas.0800202105>
- 297 Amir, R., Kinast, S., Tsoar, H., Yizhaq, H., Zaady, E., & Ashkenazy, Y. (2014). The effect
 298 of wind and precipitation on vegetation and biogenic crust covers in the sde-hallamish
 299 sand dunes. *Journal of Geophysical Research: Earth Surface*, *119*(3), 437–450. doi:
 300 <https://doi.org/10.1002/2013JF002944>
- 301 Anderson, R. S., & Haff, P. K. (1988). Simulation of eolian saltation. *Science*, *241*(4867),
 302 820–823. doi: <https://doi.org/10.1126/science.241.4867.820>
- 303 Bagnold, R. A. (1941). *The physics of blown sand and desert dunes*. Methuen, London.
- 304 Carneiro, M. V., Pätz, T., & Herrmann, H. J. (2011). Jump at the onset of saltation.
 305 *Physical Review Letters*, *107*(9), 098001. doi: [https://doi.org/10.1103/PhysRevLett](https://doi.org/10.1103/PhysRevLett.107.098001)
 306 [.107.098001](https://doi.org/10.1103/PhysRevLett.107.098001)
- 307 Cheng, N.-S. (1997). Simplified settling velocity formula for sediment particle. *Journal of*
 308 *hydraulic engineering*, *123*(2), 149–152.
- 309 Comola, F., Gaume, J., Kok, J., & Lehning, M. (2019). Cohesion-induced enhancement
 310 of aeolian saltation. *Geophysical Research Letters*, *46*(10), 5566–5574. doi: <https://doi.org/10.1029/2019GL082195>
- 311 Creyssels, M., Dupont, P., El Moctar, A. O., Valance, A., Cantat, I., Jenkins, J. T., ...
 312 Rasmussen, K. R. (2009). Saltating particles in a turbulent boundary layer: ex-
 313 periment and theory. *J. Fluid Mechanics*, *625*, 47. doi: [https://doi.org/10.1017/](https://doi.org/10.1017/S0022112008005491)
 314 [S0022112008005491](https://doi.org/10.1017/S0022112008005491)
- 315 Cundall, P. A., & Strack, O. D. (1979). A discrete numerical model for granular assemblies.
 316 *geotechnique*, *29*(1), 47–65. doi: <https://doi.org/10.1680/geot.1979.29.1.47>
- 317 De Vries, S., de Vries, J. v. T., Van Rijn, L., Arens, S., & Ranasinghe, R. (2014). Aeolian
 318 sediment transport in supply limited situations. *Aeolian Research*, *12*, 75–85. doi:
 319 <https://doi.org/10.1016/j.aeolia.2013.11.005>
- 320 Durán, O., Andreotti, B., & Claudin, P. (2012). Numerical simulation of turbulent sediment
 321 transport, from bed load to saltation. *Physics of Fluids*, *24*(10), 103306. doi: <https://doi.org/10.1063/1.4757662>
- 322 Durán, O., Parteli, E. J., & Herrmann, H. J. (2010). A continuous model for sand dunes:
 323 Review, new developments and application to barchan dunes and barchan dune fields.
 324 *Earth Surface Processes and Landforms*, *35*(13), 1591–1600. doi: <https://doi.org/10.1002/esp.2070>
- 325 Gillette, D. A. (1981). Production of dust that may be carried great distances. In *Desert*
 326 *Dust: Origin, Characteristics, and Effect on Man*. Geological Society of America. doi:
 327 <https://doi.org/10.1130/SPE186-p11>
- 328 Ho, T. D., Valance, A., Dupont, P., & El Moctar, A. O. (2011). Scaling laws in aeolian sand
 329 transport. *Physical Review Letters*, *106*(9), 094501. doi: [https://doi.org/10.1103/](https://doi.org/10.1103/PhysRevLett.106.094501)
 330 [PhysRevLett.106.094501](https://doi.org/10.1103/PhysRevLett.106.094501)
- 331 Hoonhout, B. M., & Vries, S. d. (2016). A process-based model for aeolian sediment
 332 transport and spatiotemporal varying sediment availability. *Journal of Geophys-*
 333 *ical Research: Earth Surface*, *121*(8), 1555–1575. doi: [https://doi.org/10.1002/](https://doi.org/10.1002/2015JF003692)
 334 [2015JF003692](https://doi.org/10.1002/2015JF003692)
- 335 Kok, J. F., Parteli, E. J., Michaels, T. I., & Karam, D. B. (2012). The physics of wind-blown
 336 sand and dust. *Reports on progress in Physics*, *75*(10), 106901. doi: <https://doi.org/10.1088/0034-4885/75/10/106901>
- 337
 338
 339
 340

- 341 Kok, J. F., & Renno, N. O. (2009). A comprehensive numerical model of steady state
342 saltation (comsalt). *Journal of Geophysical Research: Atmospheres*, *114*(D17). doi:
343 <https://doi.org/10.1029/2009JD011702>
- 344 Kroy, K., Sauermann, G., & Herrmann, H. J. (2002, Sep). Minimal model for aeolian sand
345 dunes. *Phys. Rev. E*, *66*, 031302. doi: <https://doi.org/10.1103/PhysRevE.66.031302>
- 346 Lämmel, M., Dzikowski, K., Kroy, K., Oger, L., & Valance, A. (2017). Grain-scale modeling
347 and splash parametrization for aeolian sand transport. *Phys. Rev. E*, *95*, 022902. doi:
348 <https://doi.org/10.1103/PhysRevE.95.022902>
- 349 Lämmel, M., Rings, D., & Kroy, K. (2012). A two-species continuum model for aeolian sand
350 transport. *The New Journal of Physics*, *14*(9), 093037. doi: <https://doi.org/10.1088/1367-2630/14/9/093037>
- 352 Li, G., Zhang, J., Herrmann, H. J., Shao, Y., & Huang, N. (2020). Study of aerody-
353 namic grain entrainment in aeolian transport. *Geophysical Research Letters*, *47*(11),
354 e2019GL086574. doi: <https://doi.org/10.1029/2019GL086574>
- 355 Macpherson, T., Nickling, W. G., Gillies, J. A., & Etyemezian, V. (2008). Dust emissions
356 from undisturbed and disturbed supply-limited desert surfaces. *Journal of Geophysical
357 Research: Earth Surface*, *113*(F2). doi: <https://doi.org/10.1029/2007JF000800>
- 358 Mahowald, N., Albani, S., Kok, J. F., Engelstaeder, S., Scanza, R., Ward, D. S., & Flanner,
359 M. G. (2014). The size distribution of desert dust aerosols and its impact on the
360 earth system. *Aeolian Research*, *15*, 53–71. doi: <https://doi.org/10.1016/j.aeolia.2013.09.002>
- 362 Owen, P. R. (1964). Saltation of uniform grains in air. *Journal of Fluid Mechanics*, *20*(2),
363 225–242. doi: <https://doi.org/10.1017/S0022112064001173>
- 364 Pähtz, T., & Durán, O. (2020). Unification of aeolian and fluvial sediment transport rate
365 from granular physics. *Physical review letters*, *124*(16), 168001. doi: <https://doi.org/10.1103/PhysRevLett.124.168001>
- 366 Pähtz, T., Liu, Y., Xia, Y., Hu, P., He, Z., & Tholen, K. (2021). Unified model of sediment
367 transport threshold and rate across weak and intense subaqueous bedload, windblown
368 sand, and windblown snow. *Journal of Geophysical Research: Earth Surface*, *126*(4),
369 e2020JF005859. doi: <https://doi.org/10.1029/2020JF005859>
- 370 Pähtz, T., Parteli, E. J. R., Kok, J. F., & Herrmann, H. J. (2014). Analytical model
371 for flux saturation in sediment transport. *Physical Review E*, *89*(5), 052213. doi:
372 <https://doi.org/10.1103/PhysRevE.89.052213>
- 373 Ralaiarisoa, J., Besnard, J.-B., Furieri, B., Dupont, P., El Moctar, A. O., Naaim-Bouvet,
374 F., & Valance, A. (2020). Transition from saltation to collisional regime in wind-
375 blown sand. *Physical Review Letters*, *124*(19), 198501. doi: <https://doi.org/10.1103/PhysRevLett.124.198501>
- 376 Sauermann, G., Kroy, K., & Herrmann, H. J. (2001). Continuum saltation model for sand
377 dunes. *Physical Review E*, *64*(3), 031305. doi: <https://doi.org/10.1103/PhysRevE.64.031305>
- 378 Schepanski, K. (2018). Transport of mineral dust and its impact on climate. *Geosciences*,
379 *8*(5). doi: <https://doi.org/10.3390/geosciences8050151>
- 380 Shao, Y. (Ed.). (2008). *Physics and modelling of wind erosion*. Springer Netherlands. doi:
381 <https://doi.org/10.1007/978-1-4020-8895-7>
- 382 Shao, Y., & Li, A. (1999). Numerical modelling of saltation in the atmospheric surface
383 layer. *Boundary-Layer Meteorology*, *91*, 199–225. doi: <https://doi.org/10.1023/A:1001816013475>
- 384 Shao, Y., Raupach, M., & Findlater, P. (1993). Effect of saltation bombardment on the
385 entrainment of dust by wind. *Journal of Geophysical Research: Atmospheres*, *98*(D7),
386 12719–12726. doi: <https://doi.org/10.1029/93JD00396>
- 387 Sørensen, M. (2004). On the rate of aeolian sand transport. *Geomorphology*, *59*(1-4), 53–62.
388 doi: <https://doi.org/10.1016/j.geomorph.2003.09.005>
- 389 Wang, X., Zhang, C., Wang, H., Qian, G., Luo, W., Lu, J., & Wang, L. (2011). The signif-
390 icance of gobi desert surfaces for dust emissions in china: an experimental study.
391 *Environmental Earth Sciences*, *64*(4), 1039–1050. doi: <https://doi.org/10.1007/>

- s12665-011-0922-2
- 396
397 Werner, B. T. (1995). Eolian dunes: computer simulations and attractor interpretation.
398 *Geology*, *23*(12), 1107–1110. doi: [https://doi.org/10.1130/0091-7613\(1995\)023\(1107:
399 EDCSAA\)2.3.CO;2](https://doi.org/10.1130/0091-7613(1995)023(1107:EDCSAA)2.3.CO;2)
- 400 Yin, X., Huang, N., Jiang, C., Parteli, E. J., & Zhang, J. (2021). Splash function for
401 the collision of sand-sized particles onto an inclined granular bed, based on discrete-
402 element-simulations. *Powder Technology*, *378*, 348-358. doi: [https://doi.org/10.1016/
403 j.powtec.2020.10.008](https://doi.org/10.1016/j.powtec.2020.10.008)

404 References from the Supporting Information

- 405 Brilliantov, N. V., Spahn, F., Hertzsch, J.-M., & Pöschel, T. (1996). Model for collisions
406 in granular gases. *Physical review E*, *53*(5), 5382. doi: [https://doi.org/10.1103/
407 PhysRevE.53.5382](https://doi.org/10.1103/PhysRevE.53.5382)
- 408 Carneiro, M. V., Araújo, N. A. M., Pähltz, T., & Herrmann, H. J. (2013). Midair collisions
409 enhance saltation. *Physical review letters*, *111*(5), 058001. doi: [https://doi.org/
410 10.1103/PhysRevLett.111.058001](https://doi.org/10.1103/PhysRevLett.111.058001)
- 411 Di Renzo, A., & Di Maio, F. P. (2004). Comparison of contact-force models for the simulation
412 of collisions in dem-based granular flow codes. *Chemical Engineering Science*, *59*(3),
413 525-541. doi: <https://doi.org/10.1016/j.ces.2003.09.037>
- 414 Fan, F., Parteli, E. J. R., & Pöschel, T. (2017). Origin of granular capillarity revealed
415 by particle-based simulations. *Phys. Rev. Lett.*, *118*, 218001. doi: [https://doi.org/
416 10.1103/PhysRevLett.118.218001](https://doi.org/10.1103/PhysRevLett.118.218001)
- 417 Fryberger, S. G., Al-Sari, A. M., Clisham, T. J., Rizvi, S. A. R., & Al-Hinai, K. G. (1984).
418 Wind sedimentation in the jafurah sand sea, saudi arabia. *Sedimentology*, *31*, 413-431.
419 doi: <https://doi.org/10.1111/j.1365-3091.1984.tb00869.x>
- 420 Kruggel-Emden, H., Simsek, E., Rickelt, S., Wirtz, S., & Scherer, V. (2007). Review and
421 extension of normal force models for the discrete element method. *Powder Technol.*,
422 *171*, 157-173. doi: <https://doi.org/10.1016/j.powtec.2006.10.004>
- 423 Luding, S. (2008). Cohesive, frictional powders: contact models for tension. *Granular
424 matter*, *10*(4), 235. doi: <https://doi.org/10.1007/s10035-008-0099-x>
- 425 Machado, M., Moreira, P., Flores, P., & Lankarani, H. M. (2012). Compliant contact force
426 models in multibody dynamics: Evolution of the hertz contact theory. *Mechanism and
427 Machine Theory*, *53*, 99-121. doi: [https://doi.org/10.1016/j.mechmachtheory.2012.02
428 .010](https://doi.org/10.1016/j.mechmachtheory.2012.02.010)
- 429 Parteli, E. J. R., Schmidt, J., Blümel, C., Wirth, K.-E., Peukert, W., & Pöschel, T. (2014).
430 Attractive particle interaction forces and packing density of fine glass powders. *Sci.
431 Rep.*, *4*, 6227. doi: <https://doi.org/10.1038/srep06227>
- 432 Plimpton, S. (1995). Fast parallel algorithms for short-range molecular dynamics. *Journal of
433 computational physics*, *117*(1), 1–19. (Website of the DEM solver LAMMPS: [https://
434 lammps.sandia.gov/](https://lammps.sandia.gov/)) doi: <https://doi.org/10.1006/jcph.1995.1039>
- 435 Pöschel, T., & Schwager, T. (2005). *Computational granular dynamics*. Springer Berlin
436 Heidelberg. doi: <https://doi.org/10.1007/3-540-27720-X>
- 437 Santos, A. P., Bolintineanu, D. S., Grest, G. S., Lechman, J. B., Plimpton, S. J., Srivastava,
438 I., & Silbert, L. E. (2020). Granular packings with sliding, rolling, and twisting friction.
439 *Phys. Rev. E*, *102*, 032903. doi: <https://doi.org/10.1103/PhysRevE.102.032903>
- 440 Schäfer, J., Dippel, S., & Wolf, D. E. (1996). Force Schemes in Simulations of Granular
441 Materials. *J. Phys. I France*, *6*, 5-20. doi: <https://doi.org/10.1051/jp1:1996129>
- 442 Schmidt, J., Parteli, E. J., Uhlmann, N., Wörlein, N., Wirth, K.-E., Pöschel, T., & Peukert,
443 W. (2020). Packings of micron-sized spherical particles: Insights from bulk density de-
444 termination, x-ray microtomography and discrete element simulations. *Advanced Pow-
445 der Technology*, *31*(6), 2293-2304. doi: <https://doi.org/10.1016/j.appt.2020.03.018>
- 446 Shao, Y., & Lu, H. (2000). A simple expression for wind erosion threshold friction velocity.
447 *Journal of Geophysical Research: Atmospheres*, *105*(D17), 22437-22443. doi: [https://
448 doi.org/10.1029/2000JD900304](https://doi.org/10.1029/2000JD900304)

- 449 Silbert, L. E., Ertas, D., Grest, G. S., Halsey, T. C., Levine, D., & Plimpton, S. J. (2001).
450 Granular flow down an inclined plane: Bagnold scaling and rheology. *Physical Review*
451 *E*, *64*(5), 051302. doi: <https://doi.org/10.1103/PhysRevE.64.051302>
452 Verbücheln, F., Parteli, E. J. R., & Pöschel, T. (2015). Helical inner-wall texture prevents
453 jamming in granular pipe flows. *Soft Matter*, *11*(21), 4295–4305. doi: [https://doi.org/](https://doi.org/10.1039/c5sm00760g)
454 [10.1039/c5sm00760g](https://doi.org/10.1039/c5sm00760g)

Supporting Information for “Scaling laws in Aeolian sand transport under low sand availability”

Sandesh Kamath^{1,2}, Yaping Shao¹, Eric J. R. Parteli²

¹Institute of Geophysics and Meteorology, University of Cologne, Germany

²Faculty of Physics, University of Duisburg-Essen, Germany

Contents of this file

Text S1 to S6

Figures S1 to S4

Table S1

Introduction

In this Supplemental Material, we briefly review the features of the Discrete-Element-Method referred to in the main document, including the complete set of the equations of motion, the details of the numerical integration of these equations, and the models of particle-particle interactions adopted in the simulations of Aeolian sand transport. Furthermore, we present the results of our numerical simulations performed to verify our model, the vertical profiles of the wind velocity and grain-borne shear stress during steady-state transport, and the behavior of the transport layer thickness as a function of the thickness of mobile sand layer, as mentioned in the main document.

S1 Discrete-Element-Method

In the Discrete-Element-Method, the equations of motion are solved for every particle in the system under consideration of the main forces acting on them. These forces are, in the process of non-suspended Aeolian transport of cohesionless particles, the drag force, the inter-particle contact forces and the gravitational force.

S1.1 Equations of motion and contact force model for the sand particles

The equation of translational motion for a particle of mass m_i at position \mathbf{r}_i reads,

$$m_i \ddot{\mathbf{r}}_i = \mathbf{F}_i^d + m_i \mathbf{g} + \sum_{\substack{1 \leq j \leq N_p \\ j \neq i}} \mathbf{F}_{ij}^c \quad (1)$$

where \mathbf{F}_i^d is the drag force on particle i , computed with the model described in the main document, \mathbf{g} is gravity, N_p is the number of particles in the system, j denotes the index of a neighbouring particle that is in contact with particle i , and \mathbf{F}_{ij}^c denotes the contact force exerted by particle j on i (with $\mathbf{F}_{ij}^c = -\mathbf{F}_{ji}^c$).

Contact between particles j and i occurs with their center-to-center distance is smaller than the sum of their radii, i.e., the contact force acts only if the particles overlap. To model the

Corresponding author: Sandesh Kamath, skamath@uni-koeln.de

33 contact force, the following equation is used to define the overlap,

$$34 \quad \delta_{ij,n} = \min \left\{ 0, \frac{1}{2} [d_i + d_j] - (\mathbf{r}_i - \mathbf{r}_j) \cdot \mathbf{e}_{ij,n} \right\} \quad (2)$$

35 where d_i and d_j are the diameters of particles i and j , respectively, $\mathbf{r}_{ij} = \mathbf{r}_i - \mathbf{r}_j$, with \mathbf{r}_j
 36 standing for the position of particle j , and $\mathbf{e}_{ij,n} = \mathbf{r}_{ij}/r_{ij}$ denotes the normal unit vector
 37 pointing from the center of particle j to the center of particle i , with $r_{ij} = |\mathbf{r}_{ij}|$.

38 There are various contact force models for application in DEM simulations, and the mod-
 39 elling of these forces is still an active matter of research (Cundall & Strack, 1979; Schäfer et
 40 al., 1996; Brilliantov et al., 1996; Silbert et al., 2001; Di Renzo & Di Maio, 2004; Pöschel &
 41 Schwager, 2005; Kruggel-Emden et al., 2007; Luding, 2008; Machado et al., 2012; Parteli et
 42 al., 2014; Fan et al., 2017; Schmidt et al., 2020; Santos et al., 2020). In our simulations, we
 43 adopt the linear spring-dashpot model, because this model has been employed in previous
 44 simulations of wind-blown sand that reproduced the scaling laws associated with Aeolian
 45 transport over fully erodible beds (Carneiro et al., 2011, 2013; Durán et al., 2012; Comola
 46 et al., 2019).

47 Specifically, \mathbf{F}_{ij}^c can be described as the sum of a normal component, $\mathbf{F}_{ij,n}^c$, and a tangential
 48 component, $\mathbf{F}_{ij,t}^c$. Each of these components encodes an elastic term and a dissipative term,
 49 while the magnitude of the tangential force is bounded by the Coulomb friction criterion.
 50 The equations for $\mathbf{F}_{ij,n}^c$ and $\mathbf{F}_{ij,t}^c$ read (Cundall & Strack, 1979; Silbert et al., 2001; Santos
 51 et al., 2020)

$$52 \quad \mathbf{F}_{ij,n}^c = k_n \delta_{ij,n} \mathbf{e}_{ij,n} - \gamma_n m_{\text{eff}} \mathbf{v}_{ij,n} \quad (3)$$

$$53 \quad \mathbf{F}_{ij,t}^c = -\min \left\{ \mu_s |\mathbf{F}_{ij,n}^c|, k_t \xi_{ij,t} + \gamma_t m_{\text{eff}} |\mathbf{v}_{ij,t}| \right\} \frac{\mathbf{v}_{ij,t}}{|\mathbf{v}_{ij,t}|} \quad (4)$$

55 where $m_{\text{eff}} = m_i m_j / (m_i + m_j)$, with m_i and m_j denoting the masses of particles i and j ,
 56 respectively, k_n , k_t , γ_n , γ_t and μ_s are model parameters, discussed in Section S1.3 below,
 57 while the relative normal velocity $\mathbf{v}_{ij,n}$ and the relative tangential velocity $\mathbf{v}_{ij,t}$ between
 58 particles i and j are computed via

$$59 \quad \mathbf{v}_{ij,n} = (\mathbf{v}_{ij} \cdot \mathbf{e}_{ij,n}) \mathbf{e}_{ij,n} \quad (5)$$

$$60 \quad \mathbf{v}_{ij,t} = \mathbf{v}_{ij} - \mathbf{v}_{ij,n} - \frac{1}{2} (\boldsymbol{\omega}_i + \boldsymbol{\omega}_j) \times (\mathbf{r}_i - \mathbf{r}_j) \quad (6)$$

62 with $\mathbf{v}_{ij} = \mathbf{v}_i - \mathbf{v}_j$ denoting the difference between the velocities of particles i and j (\mathbf{v}_i
 63 and \mathbf{v}_j , respectively), and $\boldsymbol{\omega}_i$ and $\boldsymbol{\omega}_j$ standing for their respective rotational velocities.
 64 Moreover, in Eq. (4), $\xi_{ij,t}$ is the tangential displacement accumulated as the particles are
 65 in contact. The displacement is set as zero at initiation of the contact and is computed in
 66 the reference frame of the rotating particle pair to compensate for the effect of rigid body
 67 rotations, as described in detail in previous work (Silbert et al., 2001; Santos et al., 2020).

68 The equation of rotational motion for particle i reads

$$69 \quad I_i \boldsymbol{\omega}_i = \sum_{\substack{1 \leq j \leq N_p \\ j \neq i}} \mathbf{M}_{ij} \quad (7)$$

70 with $I_i = m_i d_i^2 / 10$ and $\boldsymbol{\omega}_i$ denoting the moment of inertia and the angular velocity of
 71 particle i , respectively, and \mathbf{M}_{ij} corresponding to the torque on particle i associated with
 72 $\mathbf{F}_{ij,t}^c$.

Table S1: Parameters of the Discrete-Element-Method.

parameter	symbol	value
elastic constant for normal contact	k_n	157 N m^{-1}
elastic constant for tangential contact	k_t	52 N m^{-1}
viscoelastic damping constant for normal contact	γ_n	0.2 kg s^{-1}
viscoelastic damping constant for tangential contact	γ_t	0.2 kg s^{-1}
Coulomb coefficient of friction	μ_s	0.3
particle diameter	d_i	$[160, 240] \mu\text{m}$
particle density	ρ_p	2650 kg m^{-3}

S1.2 Contact forces between mobile and rigid particles (non-erodible elements)

The contact forces between mobile sand particles and the rigid particles constituting the roughness elements of the bed are computed using the same model as in the previous section, but considering that the rigid particles have an infinite mass (Verbücheln et al., 2015). Specifically, the normal and tangential components of the contact force from a rigid particle j on a mobile particle i are computed with Eqs. (3) and (4), respectively, by setting $m_{\text{eff}} = m_i$. Furthermore, contact forces between rigid particles are not considered.

S1.3 Model parameters

Table S1 displays the values of the parameters in Eqs. (3) and (4), i.e., the elastic constants k_n and k_t , the damping coefficients γ_n and γ_t , and the Coulomb friction coefficient, μ_s . The elastic and damping constants are taken from previous models for Aeolian sand transport over fully erodible beds (Carneiro et al., 2011, 2013; Comola et al., 2019). In particular, the elastic constant for normal contact, k_n , is estimated using $k_n = \pi d_m Y / 4$, where $d_m = 200 \mu\text{m}$ is the mean particle size adopted in our simulations, while $Y = 1 \text{ MPa}$ is the Young’s modulus adopted in previous work (Carneiro et al., 2011; Comola et al., 2019) and in our computations. Furthermore, for the elastic constant for tangential constant, we use $k_t = k_n / 3$, while the friction coefficient is consistent with values adopted previously (Comola et al., 2019).

S1.4 Numerical implementation and particle-wind coupling

To solve the equations of motion of the granular phase, we employ LAMMPS (Large-scale Atomic/Molecular Massively Parallel Simulator), which is an open source DEM solver based on MPI implementation (Plimpton, 1995). Furthermore, we have extended this solver to incorporate the hydrodynamic description of the turbulent wind flow over the granular surface, developed in previous work (Carneiro et al., 2011; Durán et al., 2012) and briefly reviewed in the main document. To this end, we have included new modules (LAMMPS “fixes”) into the granular package of the DEM solver, to set the initial (logarithmic) vertical profile of the mean horizontal wind speed, to compute the drag force, and to update this drag force and the wind profile owing to the process of momentum exchange between the particles and the wind. These modules are available from the corresponding author upon request.

S2 Validation of our simulations over fully erodible beds

To verify our numerical simulations, we compare our numerical predictions for the height-integrated mass flux (Q) of wind-blown particles over a fully erodible bed with corresponding wind-tunnel observations of this flux as a function of the wind shear velocity, u_* . We compute Q using the following equation,

$$Q = \frac{\sum_i^N m_i v_i^x}{A} \quad (8)$$

where N is the number of particles in the system, m_i and v_i^x denote the mass and horizontal speed of the i -th particle, respectively, and $A = L_x \cdot L_y$ is the horizontal area of the simulation domain. To measure this flux, we start the wind-blown transport process as described in the main document and wait until this transport achieves steady state. The typical (physical) time separating the begin of wind-blown transport from the steady state is about 2-3 seconds and independent of u_* (Carneiro et al., 2011; Durán et al., 2012; Pähz et al., 2014; Comola et al., 2019). All results reported in the present work refer to the characteristics of steady-state wind-blown transport, and denote mean quantities obtained from averaging over about 5-10 seconds during steady-state transport.

Furthermore, by suitably normalizing the steady-state flux Q , we obtain the following non-dimensional quantity,

$$\hat{Q} = \frac{Q}{\rho_p \sqrt{(s-1)gd_m^3}}, \text{ with } s = \frac{\rho_p}{\rho_f}, \quad (9)$$

which we plot in Fig. S1 as a function of the Shields number,

$$\Theta = \frac{u_*^2 \rho_f}{(\rho_p - \rho_f)gd_m} \quad (10)$$

where $\rho_p = 2650 \text{ kg/m}^3$ and $\rho_f = 1.225 \text{ kg/m}^3$ denote the densities of the particles and the air, respectively, while $d_m = 200 \mu\text{m}$ is the mean particle diameter and $g = 9.81 \text{ m/s}^2$ is gravity.

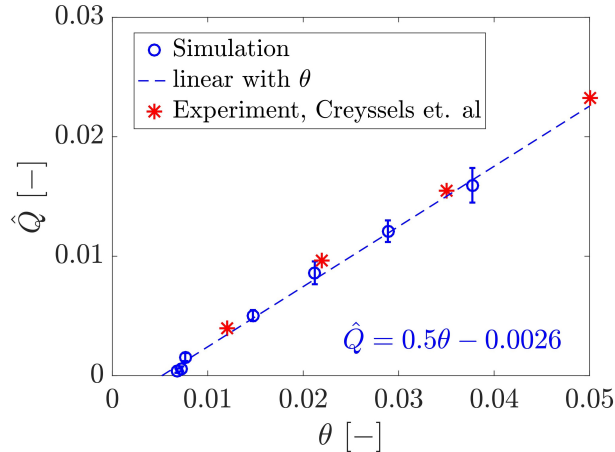


Figure S1: Normalized steady-state flux \hat{Q} as a function of the Shields number Θ , considering a fully erodible bed ($\delta_0 \approx 15 d_m$).

We see in Fig. S1 that our numerical predictions for $\hat{Q}(\Theta)$ (circles) agree quantitatively well with observations from wind-tunnel experiments (Creyssels et al., 2009), denoted by the stars. The best fit to our simulation results using $\hat{Q} = a\Theta + b$ yields $a \approx 0.5$ and $b \approx 0.0026$ (dashed line in Fig. S1), from which obtain the minimal threshold $\Theta_t \approx 0.0064$ below which

131 no transport occurs ($\hat{Q} = 0$). From Eq. (10), this value of Θ_t leads to the minimal threshold
 132 wind shear velocity for sustained transport, $u_{*t} \approx 0.165$ m/s.

133 We note that the value of u_{*t} predicted from our simulations is consistent with the prediction
 134 that u_{*t} is about 80% of the minimal threshold wind shear velocity u_{*ft} required to initiate
 135 transport,

$$136 \quad u_{*ft} = A_{ft} \sqrt{\frac{\rho_p - \rho_f}{\rho_f} g d_m}, \quad (11)$$

137 with $A_{ft} \approx 0.1$ (Bagnold, 1941; Shao & Lu, 2000). Indeed, by applying the mean particle
 138 size $d_m = 200 \mu\text{m}$ of our simulations in Eq. (11), we obtain $u_{*ft} \approx 0.206$ m/s, i.e., our model
 139 is consistent with the relation $u_{*t} \approx 0.8 u_{*ft}$ predicted for wind-blown transport.

140 S3 The modified wind profiles for varying δ_0

141 The initial vertical profile of the horizontal downstream wind velocity u_x is logarithmic and
 142 follows Eq. (3) of the main document. However, this wind velocity profile is updated every
 143 time-step, since the acceleration of the grains extracts momentum from the air thus creating
 144 a negative feedback on the wind. The modification of the wind velocity profile is computed
 145 using Eqs. (4) and (5) in the main document. The vertical profiles of the modified wind
 146 velocity u_x and the grain-borne shear stress τ_p are shown for different values of the mobile
 layer thickness δ_0 in Fig. S2.

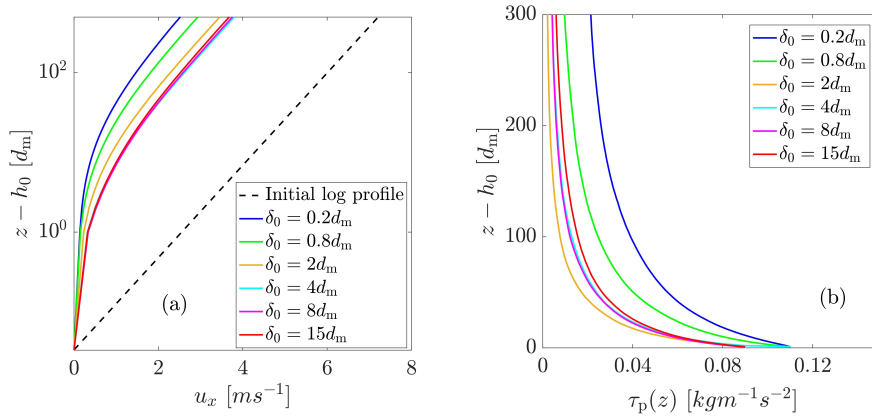


Figure S2: (a) The modified wind profiles for different values of δ_0 alongside the initial logarithmic profile; (b) grain-borne shear stress profile as a function of the height above the bed for different δ_0 . The results were obtained with $u_* = 0.30$ m/s.

147

148 S4 Computation of the mean hop length and the mean horizontal impact 149 and lift-off velocities

150 To compute the mean hop length ℓ_{hop} and the average horizontal impact and lift-off veloc-
 151 ities, $u_{0\downarrow}$ and $u_{0\uparrow}$, respectively, we consider only the grains with a minimum vertical lift-off
 152 velocity of $\sqrt{6gd}$, i.e., the grains that achieve a minimum height of $3d_m$ above the bed
 153 height. The values of ℓ_{hop} , $u_{0\downarrow}$ and $u_{0\uparrow}$, are then averaged over a time window of 5 seconds
 154 during steady-state sand transport.

155 The mean horizontal grain velocity or slip velocity u_0 is then computed using

$$156 \quad u_0 = (u_{0\downarrow} + u_{0\uparrow})/2. \quad (12)$$

157 Furthermore, to obtain the mean hop length, we start from the mean hop time, which is
 158 given by (Ho et al., 2011),

$$159 \quad t_{\text{hop}} \approx \frac{2v_{0\uparrow}}{g}, \quad (13)$$

160 where $v_{0\uparrow}$ is the mean ascending vertical velocity of the grains (also averaged over 5 seconds
 161 in the steady state). Furthermore, the horizontal acceleration of the grains is given by,

$$162 \quad a_{\text{hor}} \approx \frac{(u_{0\downarrow} - u_{0\uparrow})}{t_{\text{hop}}}, \quad (14)$$

163 so that the mean hop length is approximated as,

$$164 \quad \ell_{\text{hop}} \approx (u_{0\downarrow} - u_{0\uparrow}) \frac{v_{0\uparrow}}{g}. \quad (15)$$

165

166 **S5 Relation between the steady-state bed layer thickness, δ_s , and the** 167 **initial bed layer thickness, δ_0**

168 As mentioned in the main document, once the sand transport process begins, the initial
 169 thickness of the mobile sand bed applied in the numerical simulations, δ_0 , decreases toward
 170 a smaller value δ_s , which is achieved when transport conditions have reached steady state.
 171 As depicted in Fig. S3, δ_s and δ_0 are linearly related to each other, and the difference between
 172 both values of bed thickness displays a slight increase with u_* owing to the effect of wind
 173 shear velocity on enhancing erosion. However, we find that the scaling laws reported in
 174 the main document are valid whatever value of bed thickness is chosen, while the following
 175 relation applies,

$$176 \quad \frac{\delta_s}{d_m} = \left(\frac{\delta_0}{d_m} - C_b \frac{u_*}{\sqrt{gd_m}} \right) \cdot \Theta \left(\frac{\delta_0}{d_m} - C_b \frac{u_*}{\sqrt{gd_m}} \right) \quad (16)$$

177 where $C_b \approx 0.02$ is an empirical parameter and $\Theta(x)$ denotes the Heaviside function, i.e.,
 178 $\Theta(x) = 1$ if $x \geq 0$ and $\Theta(x) = 0$ if $x < 0$. Therefore, the term $C_b u_* / (\sqrt{gd_m})$ denotes
 179 the thickness of the total eroded layer, relative to the particle size, from the beginning of
 180 transport until steady state (i.e., as the bed thickness evolves from δ_0 toward δ_s).

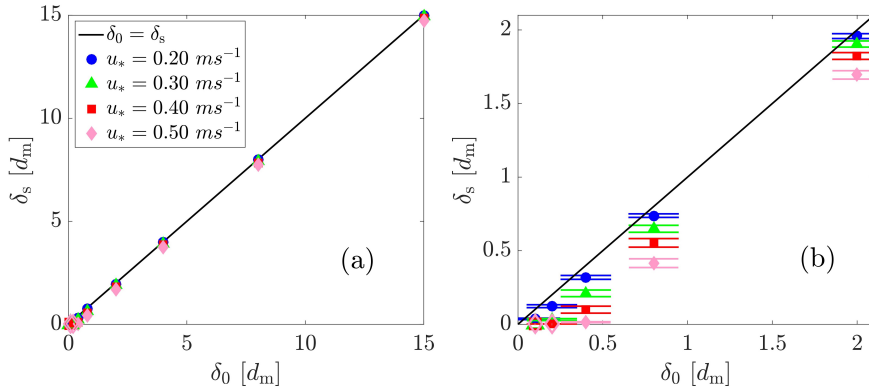


Figure S3: (a) Values of the bed layer thickness at steady-state transport, δ_s , plotted against the initial values of bed layer thickness, δ_0 , for different values of the wind shear velocity u_* . The plot in (b) denotes a zoom into the region of bed layer thickness comparable to the particle size. Filled symbols correspond to saturated transport conditions, while empty symbols denote under-saturated scenarios (the same color code used for the filled symbols in the legend applies to specify u_* in these empty symbol scenarios).

181 In Fig. S3, the filled symbols correspond to numerical simulations in which the wind is
 182 carrying the maximum possible number of particles, i.e., the flux is saturated. Starting
 183 with $\delta_0 = 15 d_m$, for instance, and under a given value of $u_* - u_{*t}$, we observe no change in
 184 the average number of particles in the Aeolian layer (or, equivalently, the mass density of
 185 dragged particles) upon a decrease in the initial bed thickness δ_0 , as long as the scenarios
 186 associated with the filled symbols in Fig. S3 are considered. However, the empty symbols
 187 in this figure constitute scenarios where the bed thickness is so small, that the wind flow
 188 does not dispose of enough particles on the ground to drive transport toward the saturated
 189 flux. These empty symbols are associated with a value of steady-state bed thickness equal
 190 to 0 and are referred to as *under-saturated*. Specifically, for these empty symbols, the wind
 191 eroded the entire sand bed and still the amount of sand transport is not enough to saturate
 192 the sand flux (the most extreme, non-vanishing flux scenario of such under-saturated regime
 193 in our simulations would be, in particular, the case of one single grain hopping downwind).

194 We have thus not considered these under-saturated scenarios in our analysis of $Q(u_*)$ in
 195 the main document, since we are interested here in an expression for the saturated flux
 196 that accounts for the bed erodibility. Moreover, it is a straightforward conclusion that,
 197 in the under-saturated regime, the mass density of the transport layer decreases upon a
 198 reduction of the initial bed thickness δ_0/d_m . Nevertheless, we note that under-saturated
 199 transport scenarios constitute an interesting topic to be investigated in future work. For
 200 instance, such scenarios have applications to areas that are devoid of any sand availability
 201 but subjected to an upwind flux that is under-saturated (for instance in the presence of
 202 upwind vegetation or moisture), or over inter-dune bedrock areas within fields of sparsely
 203 distributed dunes (Fryberger et al., 1984)).

204 S6 Transport layer thickness as a function of the bed thickness

205 As explained in the main document, the transport layer expands gradually as the soil erodi-
 206 bility conditions change from fully erodible to rigid. To quantify this process, we compute
 207 the characteristic length-scale l_ν associated with the nearly exponential decay of the particle
 208 concentration $\nu(z)$ with the height z above the ground, i.e.,

$$209 \nu(z) = \nu_0 \exp(-z/l_\nu) \quad (17)$$

210 where ν_0 is the particle concentration extrapolated to the bed ($z = 0$). Fig. S4 shows the
 211 behavior of l_ν as a function of the thickness of mobile sand layer on the ground, δ_0 . We see
 212 that, when the rigid ground is flat, l_ν decreases monotonically as δ_0 increases toward $15 d_m$
 213 (the fully erodible bed scenario). However, when the rigid surface is armoured with non-
 214 erodible elements (which in our simulations have the same size as the mobile particles), a
 215 minimum in l_ν is observed near $\delta_0 = 2 d_m$. This minimum can be explained by the prevailing
 216 occurrence of backward ejecta in the range $\delta_0 \lesssim 2 d_m$ (as described in the main document),
 217 which leads to lower values of l_ν in this range when non-erodible particles cover the ground,
 218 compared to the flat ground scenario. As δ_0 becomes much larger than the particle size, the
 219 effect of the immobile particles on the Aeolian transport thickness becomes negligible, and
 220 l_ν approaches asymptotically the value corresponding to the fully erodible bed as shown in
 221 Fig. S4.

222 References

- 223 Bagnold, R. A. (1941). *The physics of blown sand and desert dunes*. Methuen, London.
 224 Brilliantov, N. V., Spahn, F., Hertzsch, J.-M., & Pöschel, T. (1996). Model for collisions
 225 in granular gases. *Physical review E*, *53*(5), 5382. doi: [https://doi.org/10.1103/](https://doi.org/10.1103/PhysRevE.53.5382)
 226 [PhysRevE.53.5382](https://doi.org/10.1103/PhysRevE.53.5382)
 227 Carneiro, M. V., Araújo, N. A. M., Pähltz, T., & Herrmann, H. J. (2013). Midair collisions
 228 enhance saltation. *Physical review letters*, *111*(5), 058001. doi: [https://doi.org/](https://doi.org/10.1103/PhysRevLett.111.058001)
 229 [10.1103/PhysRevLett.111.058001](https://doi.org/10.1103/PhysRevLett.111.058001)

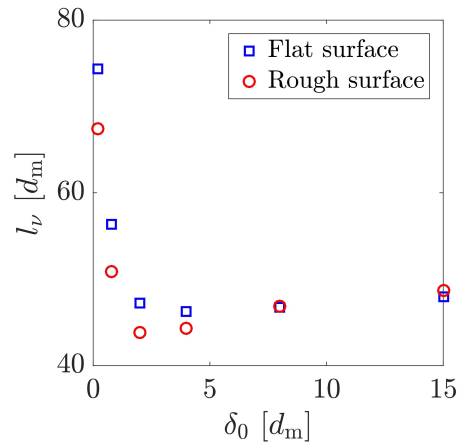


Figure S4: Thickness l_ν of the transport layer as a function of the thickness δ_0 of the mobile sediment layer covering the non-erodible surface, which consists of a flat horizontal surface (blue symbols) and a sheet of immobile particles (red symbols). The results were obtained with $u_* = 0.30$ m/s.

- 230 Carneiro, M. V., Pähtz, T., & Herrmann, H. J. (2011). Jump at the onset of saltation.
 231 *Physical Review Letters*, *107*(9), 098001. doi: [https://doi.org/10.1103/PhysRevLett](https://doi.org/10.1103/PhysRevLett.107.098001)
 232 [.107.098001](https://doi.org/10.1103/PhysRevLett.107.098001)
- 233 Comola, F., Gaume, J., Kok, J., & Lehning, M. (2019). Cohesion-induced enhancement
 234 of aeolian saltation. *Geophysical Research Letters*, *46*(10), 5566–5574. doi: [https://](https://doi.org/10.1029/2019GL082195)
 235 doi.org/10.1029/2019GL082195
- 236 Creyssels, M., Dupont, P., El Moctar, A. O., Valance, A., Cantat, I., Jenkins, J. T., ...
 237 Rasmussen, K. R. (2009). Saltating particles in a turbulent boundary layer: ex-
 238 periment and theory. *J. Fluid Mechanics*, *625*, 47. doi: [https://doi.org/10.1017/](https://doi.org/10.1017/S0022112008005491)
 239 [S0022112008005491](https://doi.org/10.1017/S0022112008005491)
- 240 Cundall, P. A., & Strack, O. D. (1979). A discrete numerical model for granular assemblies.
 241 *geotechnique*, *29*(1), 47–65. doi: <https://doi.org/10.1680/geot.1979.29.1.47>
- 242 Di Renzo, A., & Di Maio, F. P. (2004). Comparison of contact-force models for the simulation
 243 of collisions in dem-based granular flow codes. *Chemical Engineering Science*, *59*(3),
 244 525–541. doi: <https://doi.org/10.1016/j.ces.2003.09.037>
- 245 Durán, O., Andreotti, B., & Claudin, P. (2012). Numerical simulation of turbulent sediment
 246 transport, from bed load to saltation. *Physics of Fluids*, *24*(10), 103306. doi: [https://](https://doi.org/10.1063/1.4757662)
 247 doi.org/10.1063/1.4757662
- 248 Fan, F., Parteli, E. J. R., & Pöschel, T. (2017). Origin of granular capillarity revealed
 249 by particle-based simulations. *Phys. Rev. Lett.*, *118*, 218001. doi: [https://doi.org/](https://doi.org/10.1103/PhysRevLett.118.218001)
 250 [10.1103/PhysRevLett.118.218001](https://doi.org/10.1103/PhysRevLett.118.218001)
- 251 Fryberger, S. G., Al-Sari, A. M., Clisham, T. J., Rizvi, S. A. R., & Al-Hinai, K. G. (1984).
 252 Wind sedimentation in the jafurah sand sea, saudi arabia. *Sedimentology*, *31*, 413–431.
 253 doi: <https://doi.org/10.1111/j.1365-3091.1984.tb00869.x>
- 254 Ho, T. D., Valance, A., Dupont, P., & El Moctar, A. O. (2011). Scaling laws in aeolian sand
 255 transport. *Physical Review Letters*, *106*(9), 094501. doi: [https://doi.org/10.1103/](https://doi.org/10.1103/PhysRevLett.106.094501)
 256 [PhysRevLett.106.094501](https://doi.org/10.1103/PhysRevLett.106.094501)
- 257 Kruggel-Emden, H., Simsek, E., Rickelt, S., Wirtz, S., & Scherer, V. (2007). Review and
 258 extension of normal force models for the discrete element method. *Powder Technol.*,
 259 *171*, 157–173. doi: <https://doi.org/10.1016/j.powtec.2006.10.004>
- 260 Luding, S. (2008). Cohesive, frictional powders: contact models for tension. *Granular*
 261 *matter*, *10*(4), 235. doi: <https://doi.org/10.1007/s10035-008-0099-x>

- 262 Machado, M., Moreira, P., Flores, P., & Lankarani, H. M. (2012). Compliant contact force
263 models in multibody dynamics: Evolution of the hertz contact theory. *Mechanism and*
264 *Machine Theory*, *53*, 99-121. doi: <https://doi.org/10.1016/j.mechmachtheory.2012.02>
265 .010
- 266 Pähitz, T., Parteli, E. J. R., Kok, J. F., & Herrmann, H. J. (2014). Analytical model
267 for flux saturation in sediment transport. *Physical Review E*, *89*(5), 052213. doi:
268 <https://doi.org/10.1103/PhysRevE.89.052213>
- 269 Parteli, E. J. R., Schmidt, J., Blümel, C., Wirth, K.-E., Peukert, W., & Pöschel, T. (2014).
270 Attractive particle interaction forces and packing density of fine glass powders. *Sci.*
271 *Rep.*, *4*, 6227. doi: <https://doi.org/10.1038/srep06227>
- 272 Plimpton, S. (1995). Fast parallel algorithms for short-range molecular dynamics. *Journal of*
273 *computational physics*, *117*(1), 1–19. (Website of the DEM solver LAMMPS: [https://](https://lammps.sandia.gov/)
274 lammps.sandia.gov/) doi: <https://doi.org/10.1006/jcph.1995.1039>
- 275 Pöschel, T., & Schwager, T. (2005). *Computational granular dynamics*. Springer Berlin
276 Heidelberg. doi: <https://doi.org/10.1007/3-540-27720-X>
- 277 Santos, A. P., Bolintineanu, D. S., Grest, G. S., Lechman, J. B., Plimpton, S. J., Srivastava,
278 I., & Silbert, L. E. (2020). Granular packings with sliding, rolling, and twisting friction.
279 *Phys. Rev. E*, *102*, 032903. doi: <https://doi.org/10.1103/PhysRevE.102.032903>
- 280 Schäfer, J., Dippel, S., & Wolf, D. E. (1996). Force Schemes in Simulations of Granular
281 Materials. *J. Phys. I France*, *6*, 5-20. doi: <https://doi.org/10.1051/jp1:1996129>
- 282 Schmidt, J., Parteli, E. J., Uhlmann, N., Wörlein, N., Wirth, K.-E., Pöschel, T., & Peukert,
283 W. (2020). Packings of micron-sized spherical particles: Insights from bulk density de-
284 termination, x-ray microtomography and discrete element simulations. *Advanced Pow-*
285 *der Technology*, *31*(6), 2293-2304. doi: <https://doi.org/10.1016/j.appt.2020.03.018>
- 286 Shao, Y., & Lu, H. (2000). A simple expression for wind erosion threshold friction velocity.
287 *Journal of Geophysical Research: Atmospheres*, *105*(D17), 22437-22443. doi: [https://](https://doi.org/10.1029/2000JD900304)
288 doi.org/10.1029/2000JD900304
- 289 Silbert, L. E., Ertas, D., Grest, G. S., Halsey, T. C., Levine, D., & Plimpton, S. J. (2001).
290 Granular flow down an inclined plane: Bagnold scaling and rheology. *Physical Review*
291 *E*, *64*(5), 051302. doi: <https://doi.org/10.1103/PhysRevE.64.051302>
- 292 Verbücheln, F., Parteli, E. J. R., & Pöschel, T. (2015). Helical inner-wall texture prevents
293 jamming in granular pipe flows. *Soft Matter*, *11*(21), 4295–4305. doi: [https://doi.org/](https://doi.org/10.1039/c5sm00760g)
294 [10.1039/c5sm00760g](https://doi.org/10.1039/c5sm00760g)